Article

Electric Double Layer at the Rutile (110) Surface. 4. Effect of Temperature and pH on the Adsorption and Dynamics of Ions

M. Předota,*[†] M. L. Machesky,[‡] D. J. Wesolowski,[§] and P. T. Cummings[∥,⊥]

[†]Institute of Physics and Biophysics, Faculty of Science, University of South Bohemia, Branisovska 31, 370 05 Ceske Budejovice, Czech Republic

[‡]University of Illinois, Illinois State Water Survey, 2204 Griffith Drive, Champaign, Illinois 61820-7495, United States

[§]Chemical Sciences Division and [⊥]Center for Nanophase Material Sciences, Oak Ridge National Laboratory, Oak Ridge, Tennessee 37831-6110, United States

[∥]Department of Chemical and Biomolecular Engineering, Vanderbilt University, Nashville, Tennessee 37235-1604, United States

ABSTRACT: Adsorption of Rb^+, Na^+, Sr^{2+}, and Cl^- on hydroxylated (110) rutile surfaces was studied by molecular dynamics (MD) simulations. Our previous work was extended to the range of surface charge densities from −0.2 to +0.1 C/m^2 (from −0.4 to +0.1 C/m^2 for Sr^{2+}) and to temperatures of 25, 150, and 250 °C. These conditions can be linked to experimental surface charge and pH values from macroscopic titrations of rutile powders with surfaces dominated by 110 crystal planes. Simulations revealed that Na^+ and Sr^{2+} adsorb closer to the surface, shifting from predominately bidentate to tetradentate inner-sphere binding with increasing temperature, whereas Rb^+ binding is predominately tetradentate at all temperatures. These differences are related to hydration energies, which must be partially overcome for inner-sphere binding and which decrease with increasing temperature and are lowest for Rb^+. The interaction of Cl^- with the rutile surface is generally less than that for cations because of repulsion by surface oxygen atoms. These MD results provide molecular-level context for the trends observed in our corresponding macroscopic surface charge titrations. Titration curves steepen in the order $Rb^+ < Na^+ < Sr^{2+}$, reflecting the adsorption interactions related to ion charge, radius, and hydration energy.
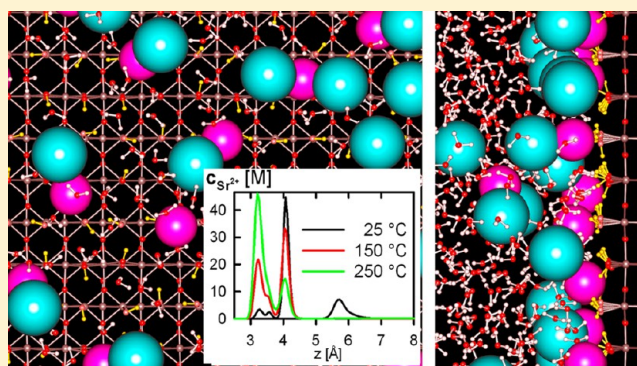
1. INTRODUCTION

Molecular dynamics (MD) simulations can provide valuable information about the structure and dynamics of water and ions near the fluid−mineral interface. Mineral surfaces contacting only pure water have been the subject of most previous MD simulations, including various oxide,[1,2] clay,[3] carbonate,[4] and sulfide[5] minerals. Simulations in which mineral surfaces are in contact with both water and ions are rarer but have included clay minerals;[6,7] cassiterite (SnO_2),[8−10] which is isostructural with rutile; SiO_2;[11] and gibbsite.[12]

In the previous articles of this series,[13−15] we described the modeling of (110) rutile (α-TiO_2) surfaces in contact with aqueous solutions and presented results on the structure of water and ions at the interface. Our MD simulation results agree very well with experimental data obtained by X-ray standing wave (XSW) and X-ray crystal truncation rod (CTR) analysis of surface structures[16,17] at ambient conditions, which can be treated as validation of our model and which enable us to extend the range of investigated properties. In this article, we investigate in detail the effects of temperature and surface charge (which is related to solution pH) on ion adsorption.

Our earlier molecular modeling results[14] focused on the adsorption of Rb^+, Na^+, Sr^{2+}, Ca^{2+}, and Zn^{2+} on neutral and negatively charged hydroxylated and nonhydroxylated 110 rutile surfaces at ambient conditions. However, as demonstrated by a number of literature studies and our own surface titration experiments with rutile powders,[9,17] both pH and temperature exert profound influences on the partitioning of ions between the solution and sorbed species. The principal effect of pH is in controlling the surface charge through surface oxygen protonation/deprotonation reactions,[20] which, in turn, provides an electrostatic driving force for ion association. Thus, in this article, we have extended our simulations to the full range of pH-induced surface charges investigated experimentally. The atomistic origins of the strong temperature dependence of ion sorption reactions, however, have heretofore remained speculative. Several short simulations at 175 °C suggested that adsorption geometries are independent of temperature, as are the distributions of ions among the various types of adsorption sites. Our much more extensive simulations detailed here confirm that the types and positions of adsorption sites are indeed temperature-independent but that the distribution of ions

among those adsorption sites generally depends on temperature. We also show that these temperature-dependent distribution changes are mirrored in our corresponding macroscopic titration results, which extends this link noted previously at 25 °C[9] to higher temperatures. We show here that ions desolvate more readily and approach the surface more closely on rutile surfaces at elevated temperatures. These findings are in accord with a recent combined experimental and modeling study of Mg^{2+}, Sr^{2+}, and Ba^{2+} adsorption on gibbsite, which showed Mg^{2+} and Sr^{2+} shifting from outer-sphere to inner-sphere binding with increasing temperature.[12] These effects are important in predicting and modeling the transport of dissolved species in deep geologic reservoirs and the synthesis and surface reactivity of oxide nanomaterials and catalytic substrates under hydrothermal conditions.

2. MOLECULAR DYNAMICS SIMULATIONS

We used the same interaction models of the surface and ions as in our previous works,[13−15] where we considered the end member surface configurations as "nonhydroxylated" (i.e., one "terminal" water molecule physisorbed at each bare Ti atom at the 110 surface, along with unprotonated "bridging" oxygens) or "hydroxylated" (i.e., dissociation of this water molecule to form OH groups at both the bridging and terminal sites). The revised results for the adsorption of ions on hydroxylated and nonhydroxylated negatively charged surfaces[15] showed that the effect of surface hydroxylation on the adsorption of ions is not as strong as originally presented in refs 13 and 14, where the results for the hydroxylated surface were affected by an error in our simulation code.[15] Therefore, in this article, we restrict ourselves to hydroxylated surfaces and three of the five originally studied cations, namely, Rb^+, Na^+, and Sr^{2+}, which represent large monovalent, small monovalent, and large divalent cations, respectively.

We have investigated the adsorption of these ions at three temperatures, namely, 25, 150, and 250 °C, and corresponding pressures of 1, 4.76, and 39.8 bar (i.e., ambient pressure at 25 °C and liquid−vapor coexistence pressures at high temperatures), for which experimental charging curves (dependence of the surface charge on solution pH) are also available.[18] These charging curves enable the effective charges at which our MD simulations are performed to be related to the surface charge and corresponding pH values observed during the course of our macroscopic titration experiments. The relation between solution pH and surface charge density from those titration experiments conducted at 0.3 m ionic strength (near the effective ionic strengths midway between the MD simulation slabs; see Table 5 below) are given in Table 1. Establishing this correspondence to experimental data is essential because the effect of pH on the interface could not be modeled directly in the current computer simulations as we used the nondissociative

SPC/E model of water,[19] which does not allow any proton transfer.

The surface species (terminal and bridging hydroxyls and their charged modifications, i.e., associated terminal water and unprotonated bridging oxygen) are set at the beginning of the simulation according to the desired surface charge density and, along with water, do not undergo any proton-exchange reactions. Starting from the fully hydroxylated neutral surface (in which each bridging oxygen is singly protonated and each 5-coordinated surface Ti^{IV} atom is bonded to terminal hydroxyl), the negative surface charge is set by manually deprotonating bridging oxygens until the desired surface charge density is reached. Positive surfaces are prepared by converting a selected number of terminal hydroxyls into associated water molecules. This scheme is consistent with our application of the revised MUSIC model[20,21] to extract individual protonation constants of bridging oxygens and terminal OH groups that define the surface charge from 25 to 250 °C. Given two surface slabs each with lateral dimensions of 35.508 Å × 38.981 Å, for example, deprotonation of 36 bridging hydrogens (i.e., 25% of the total) results in a surface charge density of −0.208 C/m^2 (for brevity, we refer to this as −0.2 C/m^2 surface charge density), and similarly for other surface charge densities (see Table 2). The

Table 2. Numbers of Protonated/Unprotonated Bridging and Terminal Groups on the Two Surfaces Forming the Slab

	surface charge density σ (C/m^2)				
group	−0.416	−0.208	−0.104	0	+0.104
unprotonated bridging O	72	36	18	0	0
protonated bridging OH	72	108	126	144	144
terminal OH	144	144	144	144	126
associated terminal H_2O	0	0	0	0	18

neutral surface is fully hydroxylated, whereas the positively charged surface with a surface charge density of +0.104 C/m^2 is prepared by replacement of 18 terminal hydroxyls with 18 associated SPC/E water molecules. Previous simulations have demonstrated that these fully associated water molecules at the terminal site do not escape from their strongly chemisorbed positions within the time frame of our simulations. However, these water molecules freely rotate and the distance between the associated water oxygen atom and the 5-fold Ti^{IV} atom at the surface remains nearly constant.

The interaction parameters between the neutral rutile surface and aqueous species were derived by ab initio calculations that were detailed previously.[22,23] The charging of the terminal and bridging surface groups was designed based on the quantum mechanical calculations of CHelpG charges of small titanium clusters.[13,22] The charge distribution scheme[13] guarantees that, even though all atoms bear only fractional charges, removal of a single bridging proton (negative surface) or removal of a terminal hydroxyl group (positive surface) decreases or increases the surface charge by exactly 1 elementary charge because of the distribution of part of the charge on variable-charge atoms, namely, terminal and bridging Ti, O, and H atoms. Table 3 summarizes the charges of all types of variable-charge atoms. The charges for σ = −0.2, −0.1, and 0 C/m^2 are identical to those presented in ref 13, whereas the charges for σ = −0.4 and +0.1 C/m^2 are newly calculated using the same charge distribution scheme. The charges of fixed-charge atoms are in all cases q_{Ti} = 2.196 e and q_O = −1.098 e.

Table 1. Relation between pH and Surface Charge Density from 0.3 m NaCl Rutile Powder Titrations

	σ (C/m^2)				
T (°C)	−0.4	−0.2	−0.1	0.0	+0.1
25	11.8[a]	8.9	7.4	5.4	<3
150	7.8	6.6	5.7	4.4	<3
250	6.5	5.6	4.9	4.1	<3

[a]Estimated pH value.

Table 3. Charges of the Variable-Charge Surface Atoms

	surface charge density σ (C/m²)				
atom charge (e)	−0.416	−0.208	−0.104	0	+0.104
surface Ti$_V$ and Ti$_{VI}$	2.112	2.134	2.146	2.196	2.167
terminal hydroxyl O	−0.984	−0.960	−0.949	−1.008	−0.928
terminal hydroxyl H	0.385	0.409	0.420	0.459	0.440
unprotonated bridging O	−1.063	−1.039	−1.028	–	–
protonated bridging O	−1.009	−0.985	−0.976	−1.035	−0.953
bridging H	0.410	0.434	0.444	0.486	0.465

The lateral distribution of these charged sites minimizes the electrostatic repulsion of the like-charged surface species (cf. Figure 2 of ref 13). In all cases, we set the separation of the two surfaces to a distance of about 50−60 Å, which is sufficient to ensure that the central region between the crystal surfaces achieves bulk fluid density. The exact separation between the surfaces is adjusted to attain system pressures (calculated from the average force exerted on the surfaces) close to those maintained during the titration experiments. The net result of these boundary conditions gives fluid densities in the central region very close to the experimental density of water at the specified pressure and temperature. For pure water, the simulated bulk densities of 993, 905, and 787 kg/m³ compare well with experimental data (997, 917, and 799 kg/m³ at 25, 150, and 250 °C, respectively[24]).

The ions are modeled identically as in our earlier studies,[13−15] that is, as Lennard-Jones (LJ) spheres with the parameter values $\sigma(Rb^+) = 3.528$ Å, $\sigma(Na^+) = 2.583$ Å, $\sigma(Sr^{2+}) = 3.314$ Å, $\sigma(Cl^-) = 4.401$ Å, and $\varepsilon = 0.1$ kcal/mol in all cases and point charges equal to the nominal charges of ions; for further details, see ref 13. In our previous studies of neutral and negatively charged surfaces, we did not consider van der Waals interaction of ions with Ti atoms, as the electrostatic repulsion between Ti and cations or between terminal and bridging O and Cl$^-$ prevents close contact of ions with Ti atoms. However, in this study, we included LJ interactions of Ti atoms with ions, because of possible close contact of Cl$^-$ with bare terminal Ti atoms on the positively charged surface. The parameters $\sigma_{Ti} = 3.2945$ Å and $\varepsilon_{Ti} = 0.033$ kcal/mol were derived from a LJ potential between Ti and the oxygen atom of a water molecule fitted to the Buckingham potential governing this interaction.[13] The Lorentz−Berthelot combining rules were used for all LJ pairs.

The numbers of ions in the aqueous phase for various surface charge densities are listed in Table 4. The total number of water molecules, terminal hydroxyls, and ions was 2048 for all simulations. Note that, when the surface charge density is changed, the number of cations and/or anions must be modified to maintain electroneutrality of the whole system. There is always an excess of neutral salt $(Me^{z+} + zCl^-)$ in the system to maintain a finite ionic strength in the center of the simulation slab near that used for the experimental surface charge titrations. However, this ionic strength is somewhat variable (0.32−0.52 M for monovalent cations and 0.25−0.39 M for Sr^{2+}, Table 5) because the reservoir size is limited (to speed up simulations) and because the number of adsorbed ions varies with both temperature and surface charge. Fortunately, the number of adsorbed ions depends primarily on surface charge rather than bulk concentration (as verified by additional simulations with different numbers of dissolved ions), so the effects of variations in the bulk concentration on the reported adsorption statistics are small. Consequently, we did not attempt to precisely correct for bulk concentration changes by adjusting the numbers of dissolved ions for each individual surface charge condition, temperature, and cation type. Rather, coarser-scale adjustments were made that increased the number of Sr^{2+} ions with increasing temperature, as well as the number of Na$^+$ ions (relative to Rb$^+$) at the −0.2 C/m² charge condition (Table 4) so as to reduce the variability in bulk concentrations among simulations (Table 5).

Table 5. Average Molarities in the Center of the Simulation Slab^a

cation	surface charge density (C/m²)	25 °C	150 °C	250 °C
Rb$^+$	−0.2	0.42	0.40	0.36
	−0.1	0.45	0.44	0.39
	0.0	0.46	0.52	0.52
	+0.1	0.50	0.45	0.40
Na$^+$	−0.2	0.40	0.35	0.32
	−0.1	0.35	0.35	0.32
	0.0	0.36	0.42	0.40
	+0.1	0.40	0.42	0.39
Sr^{2+}	−0.4	0.29	0.30	0.25
	−0.2	0.31	0.27	0.35
	−0.1	0.36	0.31	0.26
	0.0	0.39	0.31	0.36
	+0.1	0.29	0.33	0.30

^{a}Homogeneous central region with a width of 20 Å.

In our analysis, we count the number of adsorbed cations in a particular type of adsorption site. The various binding sites are identified based on the number and type of surface oxygens (bridging or terminal) directly interacting with the cation, that is, those oxygens up to the first minimum of the cation−oxygen pair correlation function. Based on this analysis, we found adsorption in the three inner-sphere sites identified earlier[14,15] and depicted in Figure 1, together with an ion adsorbing as an outer-sphere species. Closest to the surface is the tetradentate (TD) site, with the cation interacting with two terminal hydroxyl oxygens and two bridging oxygens. Both of the bridging oxygens are protonated at neutral and positive surfaces, and at least one of

Table 4. Numbers of Ions in the Simulation Box

		monovalent cations		divalent cations	
surface charge density (C/m²)	surface charge to compensate (e)	no. of Rb$^+$ or Na$^+$	no. of Cl$^-$	no. of Sr^{2+}	no. of Cl$^-$
−0.4	−72	–	–	49,^{a} 54,^{b} 63^c	26,^{a} 36,^{b} 54^c
−0.2	−36	48 (Rb$^+$), 51 (Na$^+$)	12 (for Rb$^+$), 15 (for Na$^+$)	31,^{a} 34,^{b} 45^c	26,^{a} 32,^{b} 54^c
−0.1	−18	30	12	22,^{a} 25,^{b} 27^c	26,^{a} 32,^{b} 36^c
0.0	0	18	18	13,^{a} 18,^{b} 27^c	26,^{a} 36,^{b} 54^c
+0.1	18	12	30	7,^{a} 9,^{b} 9^c	32,^{a} 36,^{b} 36^c

^{a}For $T = 25$ °C. ^{b}For $T = 150$ °C. ^{c}For $T = 250$ °C.
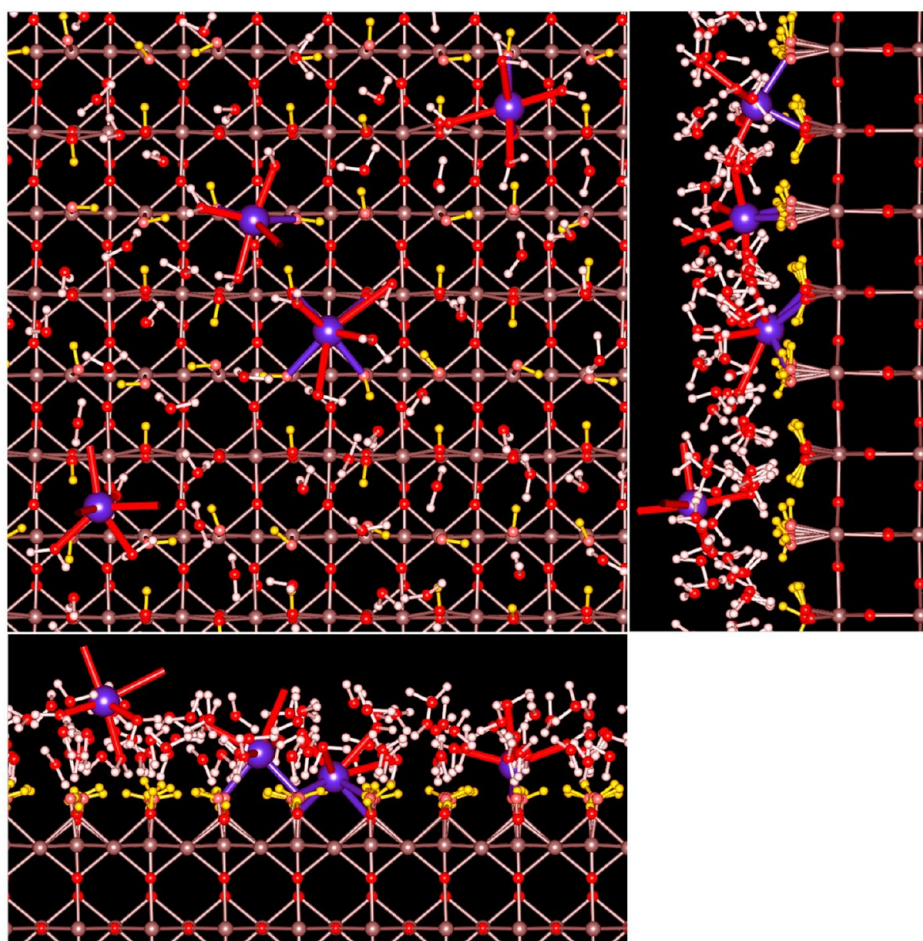
Figure 1. Negative hydroxylated surface ($\sigma = -0.2$ C/m^2) depicting, (top) from left to right in the perpendicular view, the outer-sphere, bidentate TOTO, tetradentate TD, and bidentate BOTO adsorption sites of Na$^+$ (blue). Na$^+$ coordination with surface terminal and bridging oxygens is shown in blue, and that with water oxygens is shown in red. (Bottom and upper right) The parallel views clearly indicate the relative heights of these sites. Oxygens are red with terminal oxygens shown in a lighter hue, hydrogens of water molecules are white, hydrogens of surface hydroxyls are yellow, and titanium is gray. Ions are shown in half LJ size; other atoms are scaled down for clarity. Only water molecules up to 5.9 Å from the surface and selected Na$^+$ ions are shown.

them is protonated at the negative surface because there are never two adjacent deprotonated bridging oxygens at the negative charge densities studied here. Farther from the surface is a bidentate site with a cation interacting with one bridging oxygen and one terminal oxygen; we denote this site as BOTO. The outermost inner-sphere adsorption site is a second bidentate site in which the cation interacts with two terminal oxygens (TOTO).

The three-dimensional density of adsorbed ions as a function of distance from the surface and lateral position along the surface are tallied during our simulations. From this three-dimensional information, the lateral plots of adsorbed ion density (see, e.g., Figure 2 of ref 14) can be obtained by integration over the distances from the surface, either over the entire range of interfacial distances giving rise to possible inner-sphere adsorption (about 0–5 Å depending on the ion size) or over only a narrower range of heights corresponding to a particular adsorption site. Another property obtained from the three-dimensional density is the axial density profile of ions, obtained by averaging over both lateral dimensions and giving simply the density of ions as a function of distance from the surface.

The spatial distribution of the adsorbed cations is well localized not only in the lateral density plots but also in the axial density profiles of ions, which show distinct peaks separated in

many cases by deep minima. Because these two distributions are strongly correlated, we used the positions of peaks from the axial density profiles of ions and boundaries between regions corresponding to different adsorption sites (summarized in Table 7 below) to quantify the number of ions in particular adsorption sites. The contribution of cations to each peak was analyzed in detail by directly counting cation–surface oxygen contact pairs. From this analysis, it was possible to confirm that each peak could be linked to one of the three possible adsorption sites (TD, BOTO, TOTO), except for about 4–8% of the cations, which were found to exist in various transient binding states (tridentate or monodentate). These various intermediate configurations are inevitable in MD simulations because ions jump between various sites. However, they are short-lived and ill-defined (they cannot be identified on either the axial or lateral density plots because of their considerable geometric variability), in addition to being rather infrequently observed, so they were not considered separately. In any case, of the six possible adsorption sites on (110) rutile identified by Zhang et al.,[25] only the TD, BOTO, and TOTO sites are evident in lateral density plots, and we did not observe significant monodentate adsorption at the BO or TO sites or BOBO bidentate binding (to two bridging oxygens).
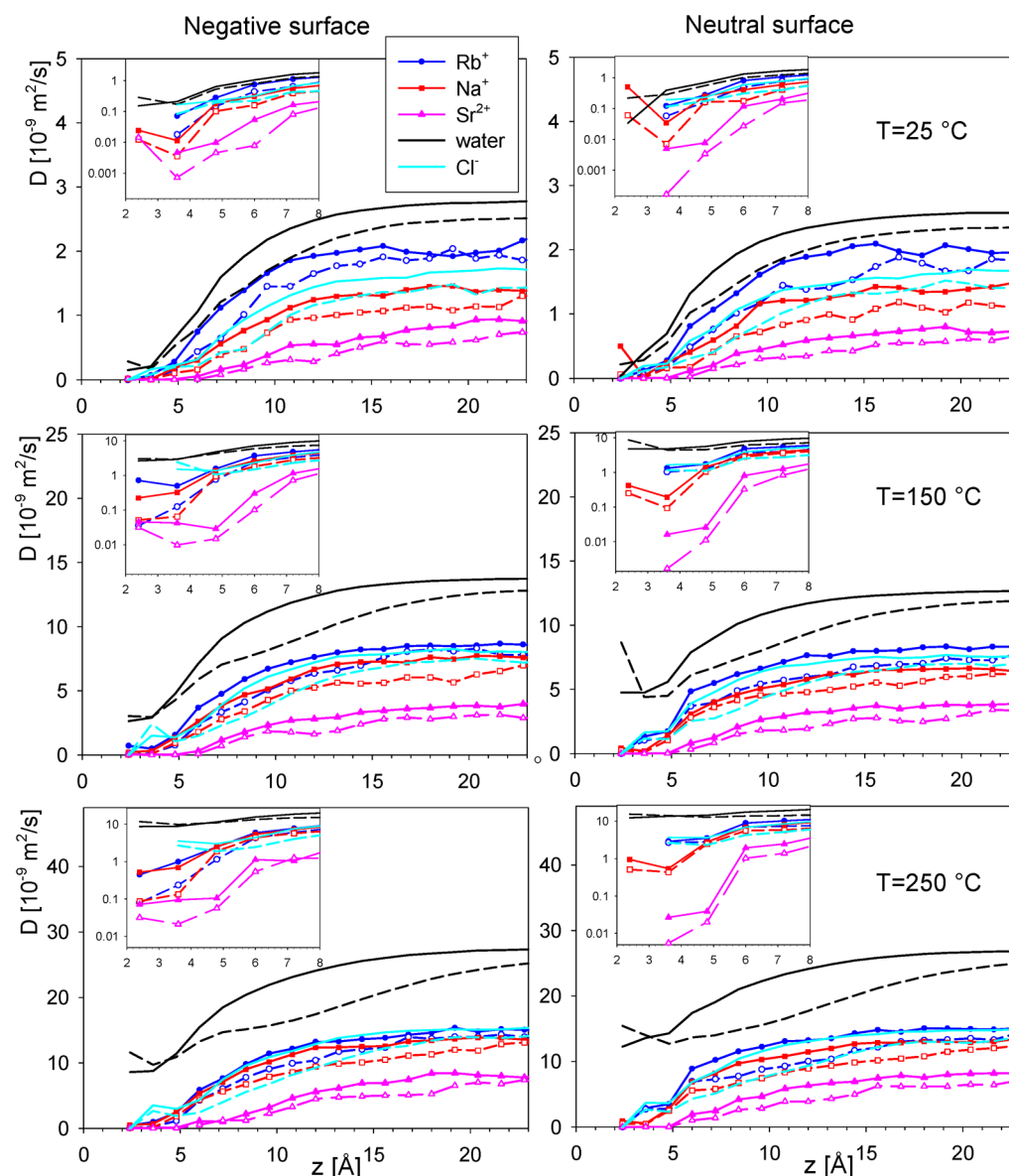
Figure 2. Diffusivities of ions and water as a function of distance z from the rutile surface for temperatures of (top) 25, (middle) 150, and (bottom) 250 °C and surface charge densities of (left) −0.2 and (right) 0 C/m^2. The parallel diffusivities are shown as solid lines with solid symbols (for the cations), perpendicular ones as dashed lines with open symbols (for the cations). The insets show the diffusivities up to 8 Å from the surface in semilogarithmic plots.

A few cations also adsorbed as outer-sphere species (not directly bound to surface oxygens), typically at heights about 6 Å above the surface Ti plane. These cations have a smeared lateral distribution but can be identified by axial density peaks. Only the first outer-sphere axial density peak was considered, because a second peak, if present (found at distances of 8−9 Å from the surface), was hardly distinguishable from the flat density profile at these and higher distances. The number of adsorbed anions and their positions are given in the form of axial density profiles and the total number of adsorbed Cl$^-$ ions up to the upper boundary of outer-sphere cations.

The mobility of cations, particularly when adsorbed on the surface, is low relative to their mobility in bulk water, as can be qualitatively observed by inspecting simulation movies of ions as a function of time, which show only infrequent jumps of adsorbed ions from one site to another, on the time scale from about 100 ps to 1 ns. Interestingly, translational jumps of second-layer water molecules, which are hydrogen-bonded to terminal and bridging oxygens, as revealed by coupled MD and quasielastic neutron scattering studies of water adsorbed on rutile nanoparticles with the (110) crystal face predominant,[26] occur at similar time scales. Quantitative results are given below in terms of diffusivity profiles of water molecules and ions as functions of distance from the surface, using the approach described previously.[13,27]

The low mobility of adsorbed ions poses convergence difficulties in obtaining reliable quantitative results for the number of adsorbed ions at each adsorption site, which is particularly important when discussing trends in occupancies as a function of temperature and pH. The convergence of a simulation was declared when two criteria were met: (i) the results did not change with increasing simulation time, and (ii) the occupancies of various types of adsorption sites on each side of the slab were similar. The fact that, in some cases, the total

number of adsorbed ions on each of the two opposing surfaces was not the same, that is, the ions did not split equally between the two surfaces, was not an obstacle. In most cases, both criteria were met within a 5-ns equilibration run, followed by at least a 5-ns production run. In instances where this was not the case, primarily for simulations of Sr^{2+} solutions at 25 °C, the simulation times were extended to 10−15 ns, and another independent simulation was started to verify/meet a third convergence criterion, namely, that (iii) the adsorption results are not affected by heating the system to the high temperature of 250 °C and cooling back to the desired temperature. In these cases, we obtained two simulations for the same thermodynamic condition. One of them (the default) was started from a random distribution of water and ions in the space between the two rutile surfaces at the desired temperature T. If there is a barrier for cations to enter the inner-sphere sites from the bulk solution (particularly for the tetradentate site, which is closest to the surface), these simulations would be expected to underpredict the number of adsorbed cations at sites closest to the surface. The other simulation was heated to 250 °C for 1 ns to accelerate the equilibration and overcome possible potential barriers. Then, the temperature was set back to the desired lower temperature T, and the system was equilibrated again for 5−15 ns. The density was fixed at the desired density for temperature T throughout this process. As will be shown below, cations adsorb more at sites closer to the surfaces at 250 °C, and therefore, when the temperature is lowered, the cations are observed to move to sites farther from the surface. If there is any potential barrier between these sites, the annealed simulations are expected to overestimate the number of ions adsorbed close to the surfaces. As these two simulations are expected to have opposite effects on the final results (because of the finite simulation time), agreement between the two simulations is treated as a stringent test that we are sampling an equilibrium configuration. The redistribution of ions (annealing of the lower-temperature structure) upon the temperature jump to 250 °C and equilibration at this temperature is so rapid that no difference between high-temperature structures was obtained by heating lower-temperature configurations or by starting from a random distribution of ions at 250 °C. Consequently, the heated, re-equilibrated, and cooled system can be treated as statistically independent from the original lower-temperature system.

3. RESULTS

3.1. Diffusivity of Ions and Water. Before describing the adsorption of ions on the rutile (110) surface as a function of temperature and surface charge (reflecting pH dependence), we discuss the inhomogeneous diffusivity profiles of water and ions. This is relevant because the diffusivities of adsorbed ions vary in the order $Rb^+ > Na^+ > Sr^{2+}$, and this must be taken into account when setting the simulation times to obtain equilibrated results. The diffusivity profiles of water and ions as functions of distance from the surface are given in Figure 2; the solid lines represent diffusivity in the xy directions parallel to the Ti surface plane, and the dashed lines represent diffusivity perpendicular to the surface. The diffusivity was calculated bin-wise from the slope of the mean square displacement versus time, as described previously.[13,27] Equidistant bins covering z = 1.8−3.0 Å, 3.0−4.2 Å, and so on, were chosen, because they roughly correspond to the first, second, and so on, layers of structured water at the interface (see Figure 4 of ref 13).

The time span for which the slope of the mean square displacement was fitted was set individually for each temperature,

because diffusivities vary significantly with temperature. The time intervals were 4−10 ps for T = 25 °C and 1−10 ps for 150 and 250 °C. These time intervals ensure that ions (and water molecules) do not diffuse far from their original positions and, therefore, that space-dependent diffusivities can be measured. By choosing such short time intervals, the effect of the finite width of the slab, which would be revealed at long times by limited maximum mean square displacement in the perpendicular dimension, is also avoided.

Our bulk diffusivities of ions and water, summarized in Table 6, agree with data from previous MD simulations[28] obtained

Table 6. Bulk Diffusivities of Water and Ions at 25 °C from Experiment (D_{exp}), Our Simulations (D_{sim}), and Reference Simulation Data[28] (D_{ref}) Using the Same Potentials

	D_{exp} ($10^{-9} m^2/s$)	D_{sim} ($10^{-9} m^2/s$)	D_{ref} ($10^{-9} m^2/s$)	ΔH_{hyd} (kJ/mol)	ΔG_{hyd} (kJ/mol)
Rb^+	2.07^a	1.97 ± 0.05	2.11 ± 0.46	−308	−281
Na^+	1.33^a	1.31 ± 0.03	1.22 ± 0.47	−416	−375
Sr^{2+}	0.79^a	0.73 ± 0.05		−1470	−1386
Cl^-	2.03^a	1.57 ± 0.02	1.73 ± 0.42	−367	−347
water	2.30^b	2.56 ± 0.05	2.59 ± 0.08		

^{a}Reference 29. ^{b}Reference 33. Experimental hydration enthalpies (ΔH_{hyd}) and Gibbs energies (ΔG_{hyd}) of ions.[32]

using the same models. The agreement with experimental values[29] is very good for Rb^+, Na^+, and Sr^{2+}. The diffusivity of Cl^- is only 75% of the experimental value, which is consistent with our unpublished results on the mobility of Cl^-, which is proportional to diffusivity according to the Nernst−Einstein equation. The diffusivity of SPC/E water is 11% higher than experimental values. The data show that the bulk diffusivities of the ions decrease in the order $Rb^+ > Cl^- > Na^+ > Sr^{2+}$ and are 1.3−3.5 times less than the bulk diffusivity of water. However, within 8 Å of the surface at 25 °C (Figure 2, top insets), the diffusivities of adsorbed Rb^+, Na^+, and Sr^{2+} are approximately 1, 2, and 3 orders of magnitude, respectively, smaller than that for water; at higher temperatures (Figure 2, middle and bottom insets), the ratios become 1 order of magnitude smaller for Na^+ and Rb^+ and 2 orders of magnitude smaller for Sr^{2+}. The diffusivities of cations at negative surfaces are slightly lower compared to those at neutral surfaces, as expected because of electrostatic forces between the surface and cations. Nevertheless, the effect of surface charge on near-surface ion mobility is minor, compared to the effect of temperature. This surprising observation, also described in our previous work, demonstrates that both the structure and the dynamics of the interfacial region are profoundly different from the behavior of the bulk electrolyte, regardless of whether the surface carries a net charge, indicating that the behavior of ions in the interfacial region has as much to do with the interfacial water structure as with the surface charge. Parallel diffusivities approach the bulk values more quickly than perpendicular ones with increasing distance from the surface. These diffusivities directly correlate with the simulation times required to obtain equilibrated ion profiles, which are shortest for Rb^+, longer for Na^+, and greatest for Sr^{2+}.

The apparent increase in diffusivity exhibited by some ions at the distance nearest the surface might signify those rare instances in which an ion enters that bin but quickly exits. The first layer of water molecules (1.8−3 Å) on negative and neutral hydroxylated surfaces is formed by dissociated water molecules (i.e., terminal hydroxyls). Occasionally (a few times during a particular

simulation), an associated SPC/E water molecule enters the first layer and contributes to the apparent increased diffusivity of water in the first layer compared to the second layer (3−4.2 Å). In fact, however, the first layer is essentially immobile over the time scales of these simulations on both hydroxylated and nonhydroxylated surfaces, as determined previously.[27] The residence time of water molecules in the first layer on the neutral nonhydroxylated surface was found to be 22 ns,[30] compared to 37.5 ps for the second layer. These residence times were obtained from the exponential fit of residence autocorrelation functions, which show the decay of the number of molecules residing in a given layer continuously for a specified time. In this way, we were able to estimate the very long residence time in the first layer, which exceeds the actual length of simulation. A similar value of 27 ns for the first layer was obtained from fitting of the intermediate scattering function predicted by MD simulations.[31] The trends observed in bulk diffusivities are in line with the hydration energies of the ions,[32] which confirm that the diffusivities decrease with increasing absolute value of hydration energy.

3.2. Adsorption of Rb⁺. The molar ion axial concentration profiles of RbCl solutions above the hydroxylated surface of rutile at the −0.2, −0.1, 0, and 0.1 C/m² charge states are shown in Figure 3. The boundaries between cation adsorption sites given in Table 7 are indicated by vertical lines in Figure 3. Identical boundaries are provided for the Cl⁻ axial profiles in Figure 3 only to facilitate comparison with the distribution of Rb⁺ (and Na⁺ in
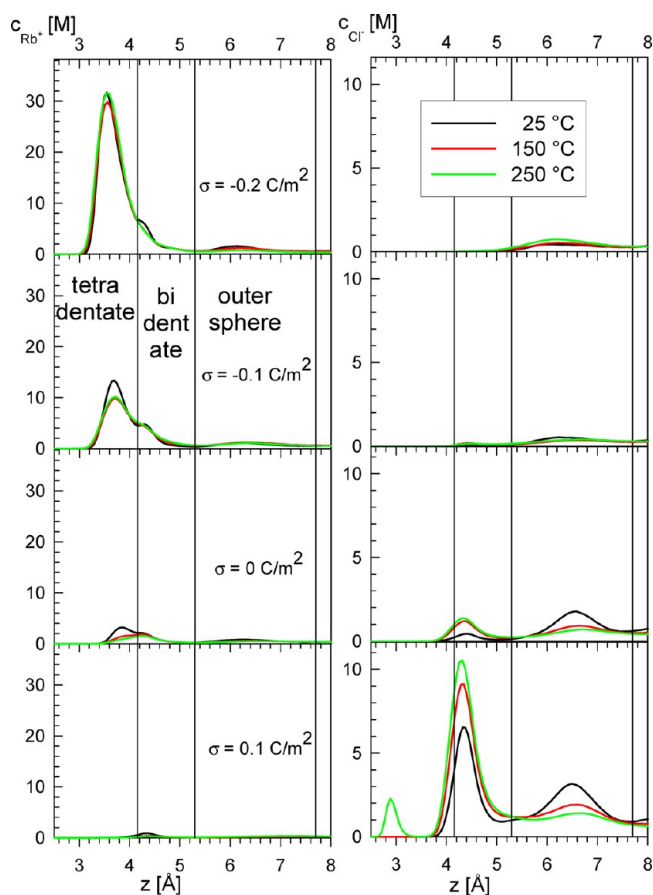
Figure 5 and Sr²⁺ in Figure 6). They do not signify binding geometry boundaries specific for Cl⁻ because those were not analyzed separately. Note that the scales for the cation and anion differ by more than a factor of 3, indicating that the concentration of sorbed Rb⁺ is much higher than that of Cl⁻ on negatively charged surfaces, comparable at neutral surfaces, and lower than that of Cl⁻ only on the positively charged surface.

The regions of tetradentate (TD) and bidentate (BD) adsorption of Rb⁺ are separated by a shallow minimum at 4.25 Å for −0.1 C/m², which largely disappears at −0.2 C/m², changing the bidentate peak to a hardly discernible shoulder of the density profile. However, the lateral distribution of the ions confirms that, in the region between heights 4.16 and 5.30 Å, both the BOTO and TOTO bidentate sites exist. This coexistence of BOTO and TOTO bidentate sites at the same height above the surface was found only for Rb⁺ and can be explained by the large size of Rb⁺ and the corresponding large position of the Rb⁺−O pair correlation function peak (not shown), which is at 2.93 Å (compared to 2.45 Å for Na⁺ and 2.64 Å for Sr²⁺). This makes Rb⁺ rather insensitive to whether the oxygen in the bidentate site is bridging or terminal.

At negative surfaces, TD adsorption strongly dominates over BD adsorption, and outer-sphere adsorption is small. The −0.1 C/m² results show much lower coverage of the TD site and nearly the same coverage of the bidentate sites as for −0.2 C/m² charge. The −0.2 C/m² density profiles are strikingly independent of temperature, even though peaks of structural distributions are generally expected to become broader and lower at higher temperatures because of increased thermal motion. Inner-sphere Rb⁺ is still present on the neutral surface (even at the TD site), but the amount decreases with temperature. On the positively charged surface, neither inner- nor outer-sphere adsorption of Rb⁺ is significant. This is entirely consistent with our bulk rutile powder titrations, which show significant sorption of Rb⁺ only at pH values above the pH of zero net proton charge.[17]

The average occupancies of the sites are reported in Table 8 for all temperatures and surface charge densities. The charge of the interface up to the outer boundary of outer-sphere adsorption (7.7 Å for Rb⁺) is given in Table 8 in the column denoted as $\sum q$ and is a measure of interfacial charge balance. This charge balance is given by the sum of the surface charge (given in parentheses in the table subheadings), the charges of inner- and outer-sphere adsorbed cations, and the negative charge of Cl⁻ within the outer-sphere boundary.

A corresponding graphical representation of the compensation of the surface charge by the distribution of ions at the interface is given in Figure 4, which depicts the integrated charge of ions up to a given distance from the surface excluding water molecule contributions. For the negative surfaces, monotonic compensation of the surface charge is observed for Rb⁺, which is the only cation for which $\sum q$ is slightly negative at negatively charged surfaces, signifying that a small fraction of the surface charge is not compensated within 7.7 Å of the surface. As commented above regarding the axial density profiles, the neutral surface at 25 °C is slightly attractive for Rb⁺ because of its interactions with bridging and terminal oxygen atoms, causing locally a small (about 0.02 C/m²) surplus of positive charge at the interface. This surplus becomes negligible at about 10 Å from the surface and decreases at higher temperatures. Traces of this behavior are observed even at the positively charged surface, where the small surplus of the positive charge at 4 Å results from Rb⁺ interacting with uncharged surface groups at heights inaccessible to the

Figure 3. Axial density profiles of (left) Rb⁺ and (right) Cl⁻ for RbCl solutions at the hydroxylated rutile (110) surface, as a function of temperature and surface charge density.

Table 7. Positions of Peaks of Axial Density Profiles of Ions and Boundaries between Regions Corresponding to Different Adsorption Sites[a]

ion	TD peak	TD–BOTO boundary	BOTO peak	BOTO–TOTO boundary	TOTO peak	TOTO–outer-sphere boundary	outer-sphere boundary
Rb+	3.55	4.16	4.25		4.25	5.3	7.7
Na+	2.90	3.13	3.25	3.50	3.75	4.75	7.0
Sr2+	3.25	3.45	3.55	3.80	4.05	4.90	7.4

[a]Heights in angstroms.

Table 8. Numbers of Cations Adsorbed in Specific Adsorption Sites for Tetradentate (TD), Bidentate Sites between Bridging and Terminal Groups (BOTO), and between Terminal Groups (TOTO) and the Outer-Sphere Boundary (OUT); Numbers of Cl⁻ Ions Counted for All Distances up to the Outer-Sphere Boundary; and Interface Charges up to the Outer-Sphere Boundary Including the Surface Charge ($\sum q$)

| ion	temperature (°C)	TD	BOTO	TOTO	OUT	Cl⁻	$\sum q$
				surface charge density = −0.4 C/m² (−72 e)			
Sr2+	25	31.4	0.5	1.4	10.5	3.1	12.5
	150	47.1	0.3	0.0	0.2	17.1	6.1
	250	55.1	0.8	0.1	0.3	38.2	2.4
				surface charge density = −0.2 C/m² (−36 e)			
Rb+	25	28.6	4.5		3.7	1.4	−0.6
	150	29.2	4.0		3.4	1.7	−1.1
	250	31.8	4.0		2.3	2.3	−0.2
Na+	25	4.5	3.7	32.3	2.0	1.7	4.8
	150	19.3	11.0	11.1	1.2	3.9	2.7
	250	22.6	11.7	7.1	1.1	4.7	1.8
Sr2+	25	1.4	0.8	16.1	6.1	3.5	9.3
	150	10.4	2.9	14.7	0.3	12.5	8.1
	250	22.8	4.9	7.6	0.6	31.5	4.3
				surface charge density = −0.1 C/m² (−18 e)			
Rb+	25	11.8	3.4		2.9	1.5	−1.4
	150	10.0	3.7		3.5	1.3	−2.1
	250	10.7	4.1		3.2	1.5	−1.5
Na+	25	0.8	2.3	17.5	1.2	1.8	2.0
	150	3.2	4.8	10.9	1.6	1.8	0.7
	250	5.1	6.1	8.2	1.6	2.5	0.5
Sr2+	25	0.0	0.0	12.0	2.4	4.4	6.4
	150	2.1	2.0	13.4	0.3	11.8	5.8
	250	4.5	2.7	12.2	0.6	18.4	3.6
				surface charge density = 0 C/m² (0 e)			
Rb+	25	2.6	1.6		2.1	4.1	2.2
	150	1.3	1.5		1.7	3.7	0.8
	250	0.9	1.3		1.6	3.6	0.2
Na+	25	0.0	0.2	8.9	1.1	4.4	5.8
	150	0.1	0.5	6.6	0.8	4.6	3.4
	250	0.1	0.6	5.7	1.0	5.4	2.0
Sr2+	25	0.0	0.0	3.7	1.1	5.3	4.3
	150	0.0	0.0	10.3	0.5	16.9	4.7
	250	0.0	0.1	17.0	0.9	32.9	3.1
				surface charge density = +0.1 C/m² (+18 e)			
Rb+	25	0.2	0.7		0.6	13.8	5.7
	150	0.1	0.3		0.7	15.3	3.8
	250	0.0	0.4		1.0	17.1	2.3
Na+	25	0.0	0.0	3.3	0.2	13.8	7.7
	150	0.0	0.0	1.2	0.4	15.0	4.6
	250	0.0	0.0	0.8	0.7	16.3	3.2
Sr2+	25	0.0	0.0	0.0	0.0	13.2	4.8
	150	0.0	0.0	0.3	0.3	16.0	3.2
	250	0.0	0.0	0.1	0.6	17.1	2.3

larger Cl⁻ ion. The surplus of Cl⁻ at greater distances, however, brings the integrated interfacial charge to neutral continuously around 12−15 Å from the surface. Charge compensation at positively charged surfaces is dominated by Cl⁻, but $\sum q$ is net positive because Cl⁻ adsorption is less than necessary to compensate the positive charge (which includes a small quantity of Rb⁺) to 7.7 Å.

3.3. Adsorption of Na⁺. The molar ion axial concentration profiles of NaCl solutions in Figure 5 show a much more complex distribution than for Rb⁺. Note again the different scales for the cation and anion. For both negative surface charge densities, the most populated adsorption site at 25 °C is the TOTO site. Increasing temperature promotes adsorption at sites closer to the surface, namely, TD and BOTO. At −0.2 C/m², the TD site becomes more populated than the TOTO site at 150 °C. However, at −0.1 C/m², even though the tendency for Na⁺ to move closer to the surface with increasing temperature is clear, the TOTO site remains dominant at all temperatures. The occupancy of the TD site is small at room temperature and remains smaller than that of the BOTO site at all temperatures. Outer-sphere adsorption of Na⁺ is very low at all temperatures, and the $\sum q$ values are positive and decrease with increasing temperature in all cases. There is a slight overcompensation of negative surface charge between about 4 and 12 Å from the surface, as shown in Figure 4.

The results presented here are consistent with our previous results[9] but disagree with recent results by Wu et al.,[11] who found 58% Na⁺ adsorption at the TD site and only 27% at the TOTO site at 25 °C and −0.2 C/m², even though they used Na⁺ potential parameters identical to ours. This discrepancy is likely due to differences in the initial configurations from which the simulations were started. Our simulations commenced from a random distribution of solution ions, whereas the simulations of Wu et al., which were concerned primarily with elucidating the effect of cations on aspartic acid binding, started with Na⁺ and the negatively charged end of aspartic acid (COO⁻) prepositioned near a deprotonated bridging oxygen. It is possible that the presence of aspartic acid, the choice of initial configurations, and the relatively short run times of 6 ns in their study were responsible for the observed predominance of TD Na⁺. We believe that our Na⁺ simulation results are accurate, at least when only Na⁺ and Cl⁻ are present.

Similarly to Rb⁺, Na⁺ readily adsorbs on the neutral surface; however, it does so significantly only at the TOTO bidentate site. We explain this difference by the smaller size and stronger hydration by water molecules around Na⁺ compared to Rb⁺. That is, the hydration sheath surrounding Na⁺ is more difficult to disrupt and remains more intact upon bidentate adsorption at the TOTO site, whereas Rb⁺ desolvation is less difficult, thereby facilitating tetradentate adsorption. We observe a statistically significant adsorption of Na⁺ at the TOTO site even on a positively charged surface. The larger affinity of Na⁺ toward the surface compared to Rb⁺ is also evident in Figure 4, with Na⁺ overcompensating the surface charge, particularly at the neutral
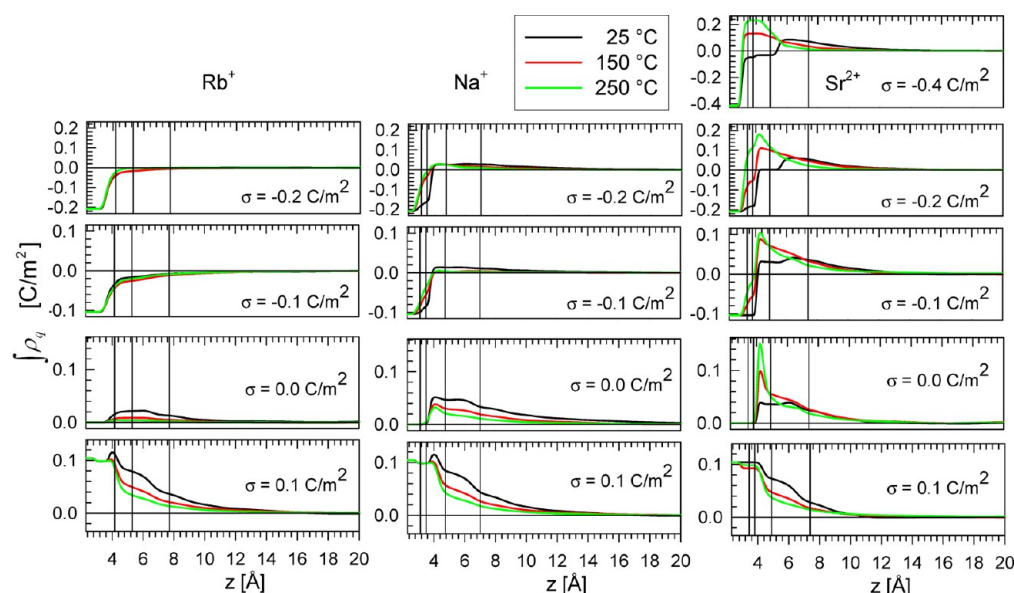
Figure 4. Integrated interfacial charge (per unit area) due to surface charge and ions. The boundaries among the identified adsorption sites are indicated by vertical lines. The contribution from water molecules is not included.
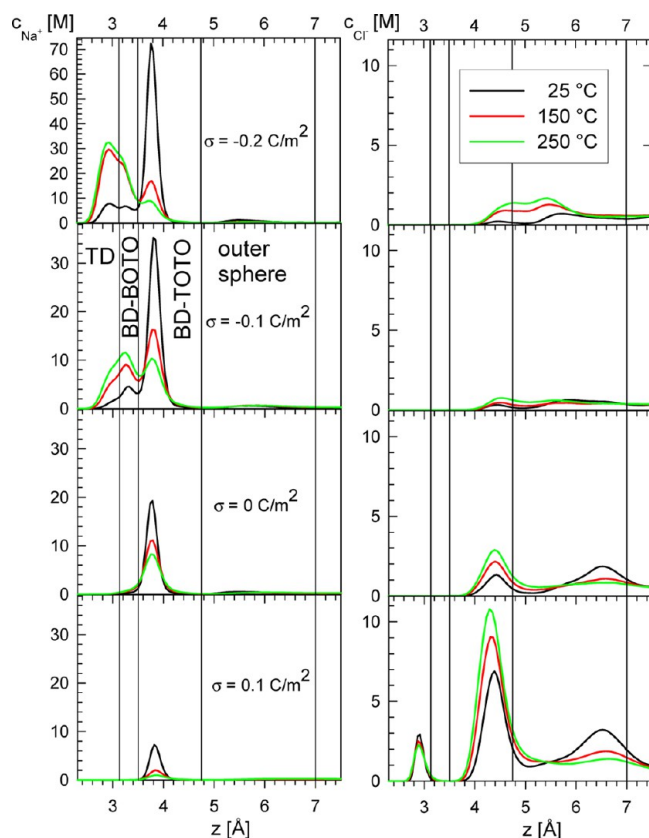
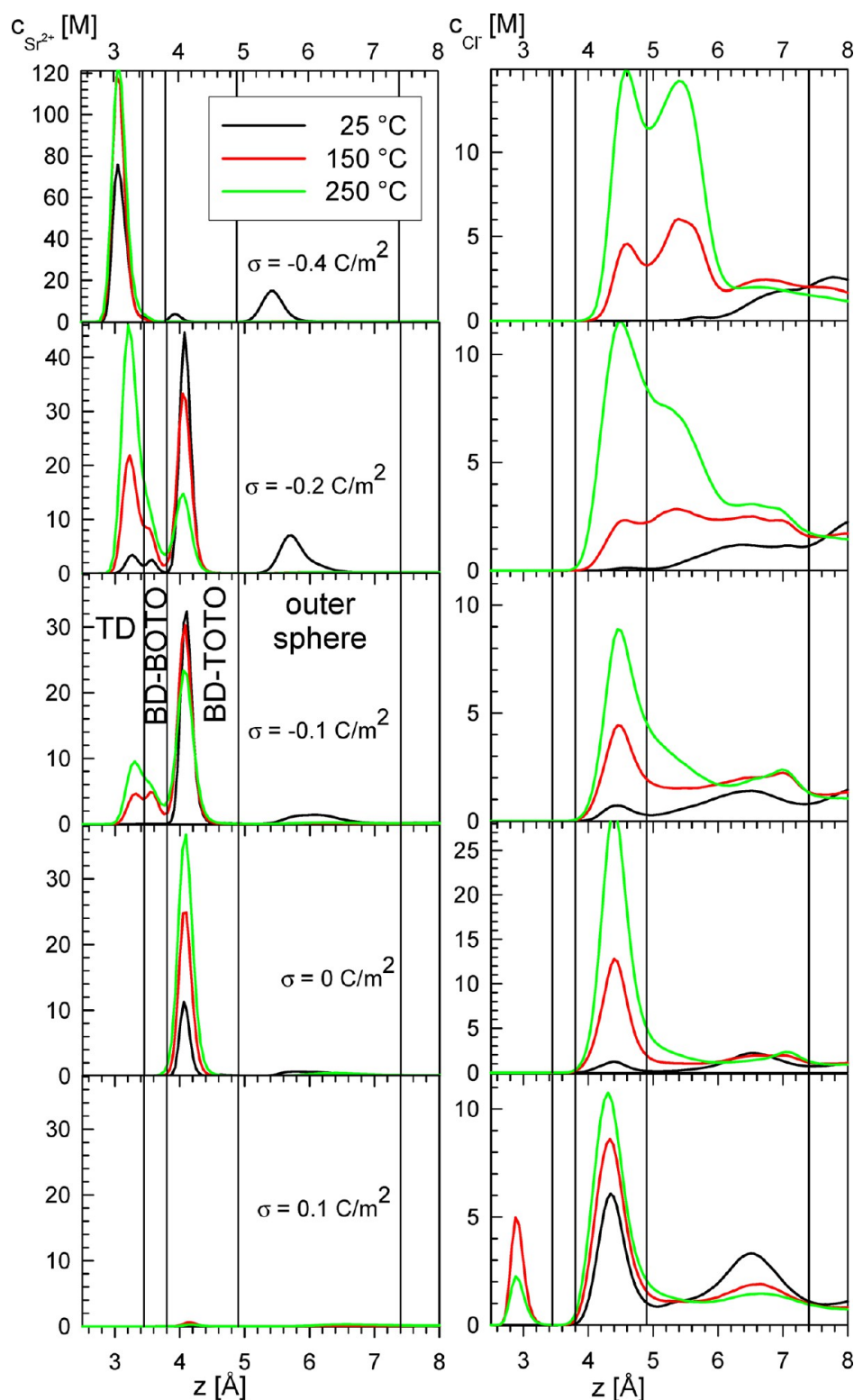**Figure 5.** Axial density profiles of (left) Na^+ and (right) Cl^-.

surface. The interfacial charge up to the outer-sphere boundary remains positive also at the positively charged surface (Table 8).

3.4. Adsorption of Sr^{2+}. As a divalent cation, Sr^{2+} is strongly solvated by water molecules, which results in its reduced mobility, even in bulk solutions, compared to Na^+ and Rb^+ (see Table 6). In the vicinity of the rutile surface, the diffusivity of Sr^{2+} is 2 orders of magnitude smaller than that of Rb^+ (Figure 2). As a result, we encountered difficulties in obtaining converged results

for Sr^{2+} adsorption from shorter 1−5-ns runs. Consequently, all Sr^{2+} results are from 10−15-ns runs. Longer run times were especially important at 25 °C, but even the 150 °C simulations converged rather slowly, until our convergence criteria, discussed above, were met.

The axial ion concentration profiles of $SrCl_2$ at the rutile surface are shown in Figure 6. At negative surfaces, Sr^{2+} shows a temperature trend similar to that of Na^+, that is, an increase in TD adsorption and a decrease in TOTO adsorption with increasing temperature, whereas BOTO adsorption remains relatively constant. For the most negative surface (-0.4 C/m²), the TD site is already dominant at 25 °C and even more so at higher temperatures, whereas for the -0.2 C/m² surface, the dominant adsorption site shifts from TOTO to TD with increasing temperature. At -0.1 C/m² charge density, the TOTO site remains dominant at all temperatures. Unlike the monovalent cations, there is significant outer-sphere adsorption at 25 °C, but at elevated temperatures, the number of Sr^{2+} adsorbed as outer-sphere species decreases to practically zero.

The -0.4 C/m² simulations resolve the discrepancy noted by Kohli et al.[34] between their resonant anomalous X-ray reflectivity results and previously available -0.2 C/m² MD results.[15] Kohli et al. found Sr^{2+} to be in predominately TD coordination above the rutile 110 surface at a height of 3.05 ± 0.16 Å, whereas previous MD results,[15] as well as those at -0.2 C/m² in Table 8, indicate significant bidentate adsorption and, hence, a considerably greater average adsorption height (3.4−3.6 Å). However, Kohli et al. conducted their X-ray experiments at pH 10.3, which, according to the 25 °C Sr^{2+} surface charge curve given in Figure 9 below, is equivalent to a surface charge of about -0.45 C/m² ($pH_{zpc} - pH = -5.1$). Consequently, the -0.4 C/m² MD results provide a better comparison, and those results indicate nearly complete TD adsorption at a height of 3.07 Å, which is in excellent agreement with the results of Kohli et al.[34] The resolution of this apparent discrepancy points to the value of macroscopic titration data. That is, without being able to confidently relate bulk solution pH to surface charge (which cannot be adequately simulated using a nondissociating water model), it would not have been possible to ascertain that the

Figure 6. Axial density profiles of (left) Sr^{2+} and (right) Cl^-.

previously available -0.2 C/m^2 MD simulations for Sr^{2+} were not an adequate comparison for the X-ray experiments. In fact, the -0.4 C/m^2 MD simulations were conducted specifically to provide a better complement for the X-ray data. Note also that the -0.4 C/m^2 surface charge shifts the position of the TD peak to 3.07 Å, whereas at smaller surface charge densities, its position is about 3.25 Å. This is direct evidence of the balance between the

attractive force of the negatively charged surface and the water hydration energy of this divalent cation.

At neutral and positive surfaces, there is no adsorption in the TD site and practically zero adsorption at the BOTO bidentate sites, which once again must be linked with a preference of Sr^{2+} to remain solvated or at most partially desolvated in the more distant binding positions.
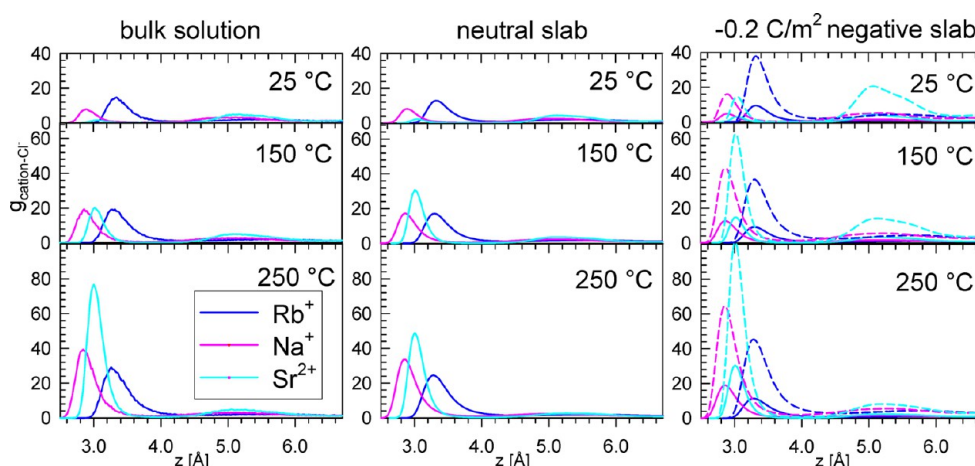
Figure 7. Cation−Cl⁻ pair correlation functions showing the contact pairs with separations smaller than about 4.5 Å and water-separated pairs around 5 Å.

3.5. Adsorption of Cl⁻.

The interactions of Cl⁻ with the surface and Cl⁻ adsorption are generally weaker than for cations because the rutile surface is terminated by exposed oxygen atoms that readily interact with cations. This electrostatic interaction is aided by the surface hydrogens being flexible enough to bend away from cations. Conversely, Cl⁻ is repelled by surface oxygen atoms and interacts only with surface and water hydrogens, which lack the axial and lateral rigidity necessary to produce specific Cl⁻ adsorption sites. An exception is on positively charged (+ 0.1 C/m²) surfaces, where 12.5% of the terminal Ti atoms are occupied by SPC/E water molecules rather than hydroxyl groups. For those simulations, terminal water molecules were sometimes replaced by Cl⁻ at a height of about 2.9 Å. This exchange was observed at all temperatures for Na⁺ as the counterion (Figure 5), at 150 and 250 °C for Sr²⁺ (Figure 6), and at 250 °C for Rb⁺ (Figure 3). The barrier associated with exchanging a terminal water molecule with Cl⁻ is rather high, which is responsible for the fact that the exchange occurred always at 250 °C but not always at lower temperatures. Such exchange was experimentally observed by IR spectroscopy following the adsorption of HCl gas.[35]

Additional axial density peaks for Cl⁻ at positive surfaces occur at about 4.4 and 6.5 Å. These peak positions are independent of the cation, and the inner peak increases in height with temperature, whereas the converse is true for the outer peak. Although we did not analyze the specific Cl⁻ binding geometries responsible for these peaks, the inner and outer peaks are due to inner-sphere and outer-sphere Cl⁻ binding, respectively. Moreover, with increasing temperature, Cl⁻ migrates closer to the positively charged surface, following the trend exhibited by cations at negatively charged surfaces.

3.6. Cation−Cl⁻ Ion Pairing.

The large amount of coadsorbed Cl⁻ in simulations with Sr²⁺ at high temperatures raises a question as to what extent this phenomenon is surface-induced or rather surface-independent, that is, related to cation−anion pairing present also in bulk systems. To answer this question, we analyzed the cation−anion pair correlation functions (Figure 7) for all cations and temperatures. Using the distance criteria summarized in Table 9, the average numbers of Cl⁻ ions in the first and second shells, that is, the numbers of contact ion pairs (CIPs) and solvent-separated ion pairs (SSIPs), respectively, are given in Table 10 for three situations.

The bulk data are from homogeneous systems without any surface and concentrations of ions close to those in the bulk part

Table 9. Positions (in Å) of Peaks and Boundaries of Contact Ion Pairs (CIPs) and Solvent-Separated Ion Pairs (SSIPs) with Cl⁻

ion	CIP peak	CIP−SSIP boundary	SSIP peak	SSIP boundary
Rb⁺	3.3	4.3	5.5	6.7
Na⁺	2.9	3.8	5.1	6.0
Sr²⁺	3.0	3.9	5.2	6.3

of our slabs, that is, 0.4 *m* for RbCl and NaCl and 0.3 *m* for SrCl₂. Figure 7 and Table 10 show that the numbers of contact pairs at 25 °C, namely, 0.44, 0.13, and 0.06 for Rb⁺, Na⁺, and Sr²⁺, respectively, decrease with increasing cation hydration energy. However, the smaller the number of CIPs at ambient conditions, the steeper its increase with increasing temperature, most prominently for Sr²⁺ at 250 °C with 1.55 Cl⁻ anions around each Sr²⁺ cation, indicating very strong ion pairing. Note that the sum of CIPs and SSIPs can exceed 2, due to sharing of Cl⁻ around several Sr²⁺ ions. An increase in Sr²⁺−Cl⁻ ion pairing with increasing temperature was also observed in the homogeneous solution MD simulations of Seward et al.[36]

The ion pairing observed in the system between neutral surfaces is very similar to that in pure bulk solution. The peaks and numbers of pairs are generally a bit smaller than in bulk solution, as might be expected due to steric restrictions around adsorbed ions, although this phenomenon is not as strong at neutral surfaces. An exception is the pairing of Sr²⁺ at 150 °C, which is stronger than in the bulk. This can be explained by quite strong bidentate (TOTO) adsorption of Sr²⁺ at this temperature (see Figure 6) and a need for interfacial Cl⁻ to compensate the charge of cations. Note that, whereas the numbers of ion pairs given in Table 10 are unequivocally determined from the analysis of simulation data, the comparison of the radial distribution functions (RDFs) in Figure 7 is subject to ambiguity, as the volume of the slab needed to normalize the RDFs is ill-defined. However, the effective volume available to the water molecules served well for this purpose.

The normalization of RDFs and even counting of the ion pairs become more complicated for charged surfaces because the numbers of ions are not in a stoichiometric ratio. For example, in a simulation of NaCl at a −0.2 C/m² surface, there are 51 Na⁺ and 15 Cl⁻ ions, that is, 36 Na⁺ cations compensating the surface charge and 15 Na⁺ and Cl⁻ ions contributing to the bulk concentration as well as interfacial concentration, depending on

Table 10. Average Numbers of Cl⁻ Ions in Contact Ion Pairs (CIPs) and Solvent-Separated Ion Pairs (SSIPs) with a Specified Cation at Temperature T

| | | homogeneous bulk | | neutral slab | | −0.2 C/m² negative slab | | | |
| | | | | | | a | | b | |
ion	T (°C)	CIP	SSIP	CIP	SSIP	CIP	SSIP	CIP	SSIP
Rb⁺	25	0.44	0.68	0.27	0.41	0.11	0.14	0.45	0.54
	150	0.58	0.61	0.35	0.38	0.12	0.14	0.48	0.57
	250	0.76	0.57	0.45	0.36	0.14	0.13	0.57	0.54
Na⁺	25	0.13	0.56	0.09	0.33	0.04	0.16	0.15	0.55
	150	0.32	0.56	0.20	0.31	0.12	0.17	0.40	0.59
	250	0.58	0.53	0.35	0.30	0.17	0.17	0.57	0.56
Sr²⁺	25	0.06	1.38	0.03	0.72	0.04	0.60	0.09	1.43
	150	0.48	1.43	0.56	0.87	0.24	0.67	0.52	1.47
	250	1.55	1.20	1.30	1.00	0.81	0.87	1.35	1.45

[a]Numbers normalized to total number of cations. [b]Numbers normalized to number of cations corresponding stoichiometrically to number of anions.

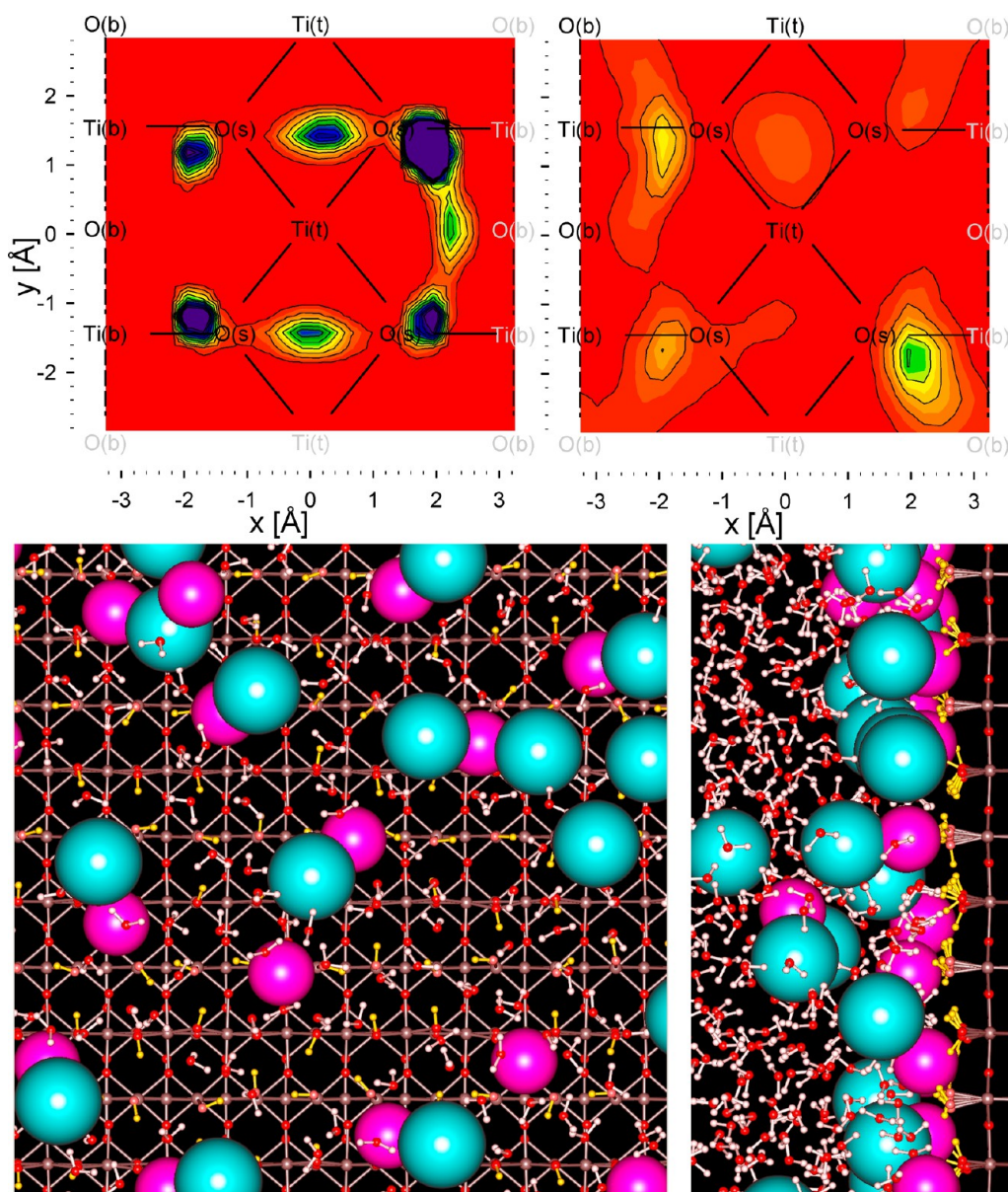**Figure 8.** (Top) Lateral distributions of (left) Sr²⁺ and (right) Cl⁻ above the hydroxylated negative surface, −0.2 C/m² and T = 250 °C at heights up to 7.6 Å above the surface. (Bottom, left) Lateral view of the same system up to 7.6 Å from the surface with Sr²⁺ in pink and Cl⁻ in cyan and (right) axial view showing the interface up to 15 Å from the surface.

their affinity toward the surface. If the total numbers of cations are used to normalize the RDFs (solid lines in the right column of Figure 7 and corresponding columns in Table 10), the values are lower compared to the bulk or a neutral slab because there are fewer anions per cation to form pairs. An opposite extreme would be to treat the cations compensating the surface charge as fully obligated to this role and not participating in ion pairing and normalize the data by the number of "free" cations, i.e., 15 in the above example (and not 51). This leads to the dashed lines in Figure 7 and the rightmost columns of Table 10. Even though the adsorbed ions have steric restrictions toward ion pairing, such pairing is present, as manifested by Figure 8. Therefore, normalization using only the numbers of free cations exaggerates the curves and values, and the effective values would lie between the two extremes presented, that is, close to those for the homogeneous bulk solution and neutral slab.

These results indicate that the large coadsorption of Cl^- observed in Figure 6 at high temperatures and quantified in Table 8 originates from strong adsorption of Sr^{2+} to neutral and even more to negative surfaces and strong formation of ion pairs at high temperatures. The tendency for $Sr^{2+}-Cl^-$ ion pairs to form appears to be no greater at the surface than in the bulk solution; that is, surface adsorption does not appear to promote ion pair formation. However, ion pairing is in competion with surface sorption, because the paired ions have lower net charge and the negatively charged surfaces that attract Sr^{2+} clearly repel Cl^- in the absence of ion pairing. Thus, sorption of Sr^{2+} would be expected to be stronger in the absence of a complexing anion, and this could also affect the distribution of this cation at various inner-sphere sites on the surface.

The distances between paired ions around 3 Å (CIP) and 5 Å (SSIP), as given in Table 9, are large enough to allow the anions to be associated with an adsorbed cation and stay a bit farther from the surface, giving rise to the local overcompensation of the interfacial charge evident in Figure 4 on a comparable scale. Figure 8 (top) depicts the lateral distribution of Sr^{2+} and Cl^- adsorption at 250 °C and -0.2 C/m^2. The lateral distribution of Cl^- indicates a preference of Cl^- to be found above the TD site. However, the snapshot (Figure 8, bottom) shows that the coadsorbed Cl^- ions do not sit directly above adsorbed Sr^{2+} ions but are laterally offset from the Sr^{2+} positions and lie closer to the surface than would be possible if they were adsorbed directly atop Sr^{2+} ions. These offset positions are stabilized by favorable interactions with both surface hydrogens and adjacent adsorbed Sr^{2+} ions, although not all adsorbed Sr^{2+} ions have a Cl^- ion in close proximity.

Na^+ shows trends in ion pairing with increasing temperature similar to those of Sr^{2+}, but Rb^+-Cl^- ion pairing is nearly temperature-independent.

3.7. Comparison to Macroscopic Titration Curves. The MD results provide molecular-level rationalization for the charge and temperature trends observed in corresponding surface charge titration curves for Rb^+, Na^+, and Sr^{2+}, which are summarized graphically in Figure 9. Titrations were conducted on a commercial rutile powder with a specific surface area of ~15 m^2/g and with the 110 crystal face predominant, following previously published methods, which included the use of stirred hydrogen electrode concentration cells above 50 °C.[18] The results are presented as surface charge normalized to surface area (σ_H, C/m^2) against pH normalized for the temperature-dependent point of zero net proton charge (pH_{znpc}) of the rutile powder ($pH_{znpc} - pH$).[21] These pH_{znpc} values are 5.4, 4.4, and 4.2 at 25, 150, and 250 °C, respectively.[20] A convenient result is
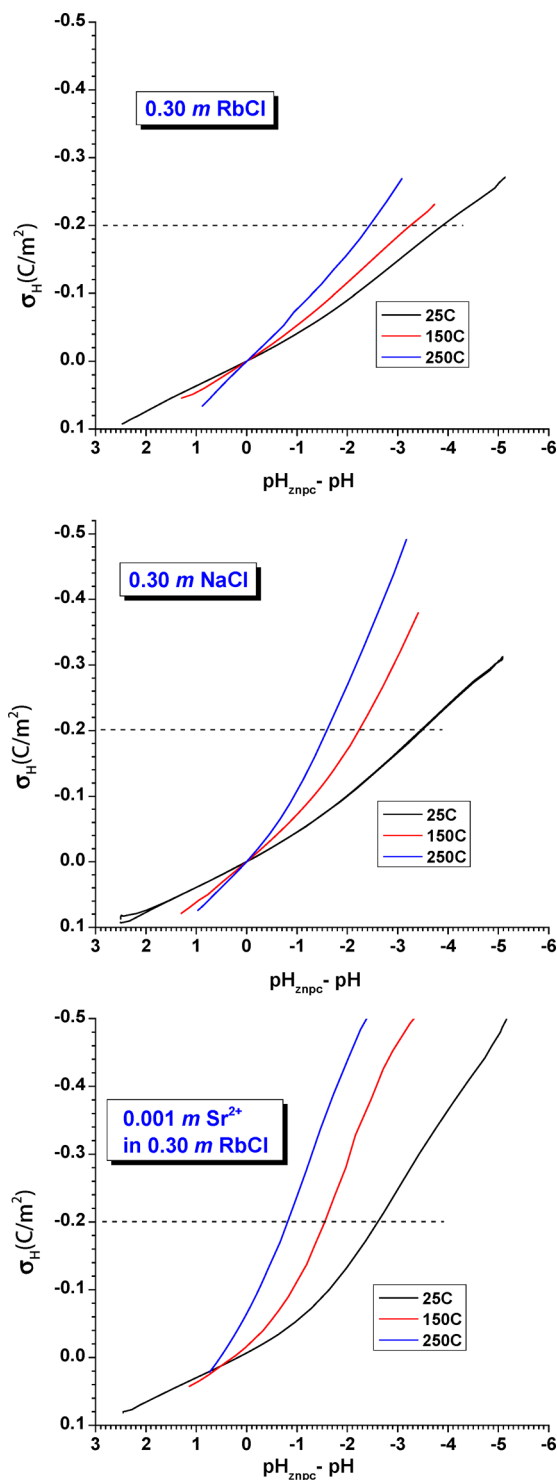
Figure 9. Surface charge (σ_H) vs $pH_{znpc} - pH$ at 25, 150, and 250 °C for (top) RbCl (0.3 m), (middle) NaCl (0.3 m), and (bottom) Sr^{2+} (0.001 m in 0.30 m RbCl).

that negative $pH_{znpc} - pH$ values correspond to negative surface charge and positive $pH_{znpc} - pH$ values to positive surface charge.

Titration curves steepen with increasing temperature for all three cations, especially at negative surface charge conditions ($pH_{znpc} - pH < 0$). This is a manifestation of Rb^+, Na^+, and Sr^{2+} being bound more closely to the rutile surface than Cl^- at an equivalent surface charge. Hence, these cations are more effective at screening surface charge development than is Cl^-, and our MD

results quantify this difference. For example, at -0.1 C/m^2, Rb$^+$ binding is predominately tetrahedral at 3.55 Å above the rutile surface, whereas at 0.1 C/m^2, fewer Cl$^-$ ions are in inner-sphere coordination, and they are farther from the surface ($\sim$4.25 Å) in bidentate coordination (Figure 3).

At negative charge conditions, titration curve slopes increase in the order Rb$^+$ < Na$^+$ < Sr^{2+} at all three temperatures, which reflects the bare ionic radii, charges, and hydration energies of these cations. For any given inner-sphere coordination mode, the larger Rb$^+$ cation is farther from the surface than are Na$^+$ and Sr^{2+}, which have smaller ionic radii (Table 7). Finally, even relatively small amounts of Sr^{2+} (0.001 m) result in the appreciable negative charge development because of its 2+ charge and because the extent of tetradentate binding increases with both temperature and negative charge.

The effect of temperature on negative surface charge development is smaller for Rb$^+$ than Na$^+$, and the MD results reveal why. Tetradentate binding predominates at all temperatures for Rb$^+$, whereas Na$^+$ shifts from predominately bidentate to tetradentate binding between 25 and 250 °C (Table 8). This shift closer to the rutile surface results in more effective screening of the negative surface charge, and hence, the surface charge curves steepen with increasing temperature. Conversely, Rb$^+$ titration curves steepen less with temperature because tetradentate binding always predominates.

4. CONCLUSIONS

This study clarifies how surface structure and charge, temperature, and ion properties influence ion adsorption phenomena at a model oxide surface (rutile 110). Our previous MD results[13−15] obtained at 25 °C and validated by X-ray reflectivity studies of rutile (110) single-crystal surfaces in contact with bulk electrolytes[16,17,25,34] were extended to higher temperatures. New sets of simulations at surface charge densities of -0.4 and $+0.1$ C/m^2 were also carried out, extending the modeled surfaces to a wider range of corresponding experimental pH conditions (from <3 to >10 at room temperature). Profiles of ion diffusivity parallel and perpendicular to the surface as functions of distance from the surface were also obtained, and those profiles confirmed the restricted motion of ions near the interface.

The MD results show that Rb$^+$, Na$^+$, and Sr^{2+} adsorb in predominately inner-sphere fashion at the negatively charged rutile (110) surface and that inner-sphere binding persists even at the neutral surface. Furthermore, the cations sorb at specific sites, progressively closer to the Ti surface plane with increasing temperature and decreasing ion hydration energy. The tetradentate (TD) site closest to the surface involves two bridging and two terminal oxygens of the surface and requires loss of four waters of hydration from the cation in forming the surface complex. Two bidentate sites (BOTO and TOTO) lie progressively farther from the surface plane, involving one bridging and one terminal oxygens and two terminal oxygens, respectively, and require loss of only two cation waters of hydration to form. Outer-sphere binding is also evident, with zero denticity and no loss of ion waters of hydration, and thus, this type of site lies much farther from the surface plane and is greatly diminished at elevated temperatures. A final type of absorption involves replacement of terminal oxygens by Cl$^-$ anions on the positively charged surface. Other than this specific site, Cl$^-$ sorption is not laterally well-defined on rutile (110). The occupancy of these specific sorption sites by individual ions results from a complex interplay among ion size and hydration energy, pH, induced surface charge, and temperature.

For Rb$^+$, tetradentate binding is the most favorable (innermost) adsorption geometry on the rutile (110) surface and always predominates because waters of hydration are relatively easily removed from this large monovalent cation. Similarly, Ba^{2+} was shown to adsorb in primarily inner-sphere fashion to the gibbsite surface because of its relatively large size and low hydration energy.[12] Conversely, Na$^+$ and Sr^{2+} bind in bidentate fashion at lower temperature and surface charge, but shift to tetradentate binding as higher temperatures and/or increasing negative surface charge promote additional release of solvation water. The -0.4 C/m^2 Sr^{2+} simulations at 25 °C (and higher temperatures) revealed predominately tetradentate binding, resolving an apparent discrepancy with X-ray reflectivity results.[17,34] Strong Sr^{2+}−Cl$^-$ ion pairing was found at higher temperatures; however, its extent is comparable to that in bulk solution, as revealed by our detailed analysis.

Macroscopic surface charge titration data were shown to qualitatively reflect the MD results. Titration curves are steeper at negative than positive charge conditions, mirroring the stronger binding of Rb$^+$, Na$^+$, and Sr^{2+} relative to Cl$^-$ found in the MD simulations. Similarly, titration curves steepen less dramatically with increasing temperature in the presence of Rb$^+$ because tetradentate binding predominates at all temperatures, whereas curves steepen more for Na$^+$ and Sr^{2+} as they move from more distant outer-sphere to bidentate and tetradentate binding with increasing temperature. Future contributions will quantitatively link these MD and surface charge titration results through the use of surface complexation models[37] that are constrained by the MD results.[38−40] These results clearly illustrate the enormous improvement in our quantitative understanding of the molecular-scale structure and diffusional dynamics of water and ions at mineral−electrolyte interfaces, as compared with continuum-based Gouy−Chapman−Stern-type surface complexation models of the electrical double layer.

■ AUTHOR INFORMATION

Corresponding Author
*E-mail: predota@prf.jcu.cz.

Notes
The authors declare no competing financial interest.

■ REFERENCES

(1) Kavathekar, R. S.; Dev, P.; English, N. J.; MacElroy, J. M. D. Molecular dynamics study of water in contact with the TiO$_2$ rutile-110, 100, 101, 001 and anatase-101, 001 surface. *Mol. Phys.* **2011**, *109*, 1649−1656.

(2) Koparde, V. N.; Cummings, P. T. Molecular Dynamics Study of Water Adsorption on TiO$_2$ Nanoparticles. *J. Phys. Chem. C* **2007**, *111*, 6920−6926.

(3) Wang, J.; Kalinichev, A. G.; Kirkpatrick, R. J. Effects of substrate structure and composition on the structure, dynamics, and energetics of water at mineral surfaces: A molecular dynamics modeling study. *Geochim. Cosmochim. Acta* **2006**, *70*, 562−582.

(4) Wolthers, M.; Di Tommaso, D.; Du, Z.; de Leeuw, N. H. Calcite surface structure and reactivity: Molecular dynamics simulations and

macroscopic surface modelling of the calcite–water interface. *Phys. Chem. Chem. Phys.* **2012**, *14*, 15145–15157.

(5) Philpott, M. R.; Goliney, I. Y.; Lin, T. T. Molecular dynamics simulation of water in a contact with an iron pyrite FeS$_2$ surface. *J. Chem. Phys.* **2004**, *120*, 1943–1950.

(6) Tournassat, C.; Chapron, Y.; Leroy, P.; Bizi, M.; Boulahya, F. Comparison of molecular dynamics simulations with triple layer and modified Gouy–Chapman models in a 0.1 M NaCl–montmorillonite system. *J. Colloid Interface Sci.* **2009**, *339*, 533–541.

(7) Bourg, I. C.; Sposito, G. Molecular dynamics simulations of the electrical double layer on smectite surfaces contacting concentrated mixed electrolyte (NaCl–CaCl$_2$) solutions. *J. Colloid Interface Sci.* **2011**, *360*, 701–715.

(8) Rosenqvist, J.; Machesky, M. L.; Vlcek, L.; Cummings, P. T.; Wesolowski, D. J. Charging Properties of Cassiterite (α-SnO$_2$) Surfaces in NaCl and RbCl Ionic Media. *Langmuir* **2009**, *25*, 10852–10862.

(9) Machesky, M.; Wesolowski, D.; Rosenqvist, J.; Předota, M.; Vlcek, L.; Ridley, M.; Kohli, V.; Zhang, Z.; Fenter, P.; Cummings, P.; Lvov, S.; Fedkin, M.; Rodriguez-Santiago, V.; Kubicki, J.; Bandura, A. Comparison of Cation Adsorption by Isostructural Rutile and Cassiterite. *Langmuir* **2011**, *27*, 4585–4593.

(10) Vlcek, L.; Zhang, Z.; Machesky, M. L.; Fenter, P.; Rosenqvist, J.; Wesolowski, D. J.; Anovitz, L. M.; Predota, M.; Cummings, P. T. Electric Double Layer at Metal Oxide Surfaces: Static Properties of the Cassiterite–Water Interface. *Langmuir* **2007**, *23*, 4925–4937.

(11) Wu, C.; Skelton, A. A.; Chen, M.; Vlček, L.; Cummings, P. T. Modeling the Interaction between Integrin-Binding Peptide (RGD) and Rutile Surface: The Effect of Cation Mediation on Asp Adsorption. *Langmuir* **2012**, *28*, 2799–2811.

(12) Katz, L. E.; Criscenti, L. J.; Chen, C.-c.; Larentzos, J. P.; Liljestrand, H. M. Temperature effects on alkaline earth metal ions adsorption on gibbsite: Approaches from macroscopic sorption experiments and molecular dynamics simulations. *J. Colloid Interface Sci.* **2013**, *399*, 68–76.

(13) Předota, M.; Bandura, A. V.; Cummings, P. T.; Kubicki, J. D.; Wesolowski, D. J.; Chialvo, A. A.; Machesky, M. L. Electric Double Layer at the Rutile (110) Surface. 1. Structure of Surfaces and Interfacial Water from Molecular Dynamics by Use of ab Initio Potentials. *J. Phys. Chem. B* **2004**, *108*, 12049–12060.

(14) Předota, M.; Zhang, Z.; Fenter, P.; Wesolowski, D. J.; Cummings, P. T. Electric Double Layer at the Rutile (110) Surface. 2. Adsorption of Ions from Molecular Dynamics and X-ray Experiments. *J. Phys. Chem. B* **2004**, *108*, 12061–12072.

(15) Předota, M.; Vlcek, L. Comment on Parts 1 and 2 of the Series "Electric Double Layer at the Rutile (110) Surface". *J. Phys. Chem. B* **2007**, *111*, 1245–1247.

(16) Zhang, Z.; Fenter, P.; Cheng, L.; Sturchio, N. C.; Bedzyk, M. J.; Machesky, M. L.; Wesolowski, D. J. Model-independent X-ray imaging of adsorbed cations at the crystal–water interface. *Surf. Sci.* **2004**, *554*, L95–L100.

(17) Zhang, Z.; Fenter, P.; Cheng, L.; Sturchio, N. C.; Bedzyk, M. J.; Předota, M.; Bandura, A.; Kubicki, O. J. D.; Lvov, S. N.; Cummings, P. T.; Chialvo, A. A.; Ridley, M. K.; Bénézeth, P.; Anovitz, L.; Palmer, D. A.; Machesky, M. L.; Wesolowski, D. J. Ion Adsorption at the Rutile–Water Interface: Linking Molecular and Macroscopic Properties. *Langmuir* **2004**, *20*, 4954–4969.

(18) Machesky, M. L.; Wesolowski, D. J.; Palmer, D. A.; Ridley, M. K.; Benezeth, P.; Lvov, S. N.; Fedkin, M. V. Ion adsorption into the hydrothermal regime: Experimental and modeling approaches. *Interface Sci. Technol.* **2006**, *11*, 324–358.

(19) Berendsen, H. J. C.; Grigera, J. R.; Straatsma, T. P. The missing term in effective pair potentials. *J. Phys. Chem.* **1987**, *91*, 6269–6271.

(20) Machesky, M. L.; Wesolowski, D. J.; Palmer, D. A.; Ridley, M. K. On the temperature dependence of intrinsic surface protonation equilibrium constants: An extension of the revised MUSIC model. *J. Colloid Interface Sci.* **2001**, *239*, 314–327.

(21) Machesky, M. L.; Predota, M.; Wesolowski, D. J.; Vlcek, L.; Cummings, P. T.; Rosenqvist, J.; Ridley, M. K.; Kubicki, J. D.; Bandura, A. V.; Kumar, N.; Sofo, J. O. Surface Protonation at the Rutile (110) Interface: Explicit Incorporation of Solvation Structure within the Refined MUSIC Model Framework. *Langmuir* **2008**, *24*, 12331–12339.

(22) Bandura, A. V.; Kubicki, J. D. Derivation of Force Field Parameters for TiO$_2$–H$_2$O Systems from ab Initio Calculations. *J. Phys. Chem. B* **2003**, *107*, 11072–11081.

(23) Bandura, A. V.; Sykes, D. G.; Shapovalov, V.; Troung, T. N.; Kubicki, J. D.; Evarestov, R. A. Adsorption of Water on the TiO$_2$ (Rutile) (110) Surface: A Comparison of Periodic and Embedded Cluster Calculations. *J. Phys. Chem. B* **2004**, *108*, 7844–7853.

(24) Lemmon, E. W.; McLinden, M. O.; Friend, D. G. In *NIST Chemistry WebBook*; NIST Standard Reference Database 69; Lindstrom, P. J., Mallard, W. G., Eds.; National Institute of Standards and Technology: Gaithersburg, MD, 2011.

(25) Zhang, Z.; Fenter, P.; Sturchio, N. C.; Bedzyk, M. J.; Machesky, M. L.; Wesolowski, D. J. Structure of rutile TiO$_2$ (1 1 0) in water and 1 molal Rb$^+$ at pH 12: Inter-relationship among surface charge, interfacial hydration structure, and substrate structural displacements. *Surf. Sci.* **2007**, *601*, 1129–1143.

(26) Mamontov, E.; Vlcek, L.; Wesolowski, D. J.; Cummings, P. T.; Wang, W.; Anovitz, L. M.; Rosenqvist, J.; Brown, C. M.; Garcia Sakai, V. Dynamics and Structure of Hydration Water on Rutile and Cassiterite Nanopowders Studied by Quasielastic Neutron Scattering and Molecular Dynamics Simulations. *J. Phys. Chem. C* **2007**, *111*, 4328–4341.

(27) Předota, M.; Cummings, P. T.; Wesolowski, D. J. Electric Double Layer at the Rutile (110) Surface. 3. Inhomogeneous Viscosity and Diffusivity Measurement by Computer Simulations. *J. Phys. Chem. B* **2007**, *111*, 3071–3079.

(28) Lee, S. H.; Rasaiah, J. C. Molecular Dynamics Simulation of Ion Mobility. 2. Alkali Metal and Halide Ions Using the SPC/E Model for Water at 25 °C. *J. Phys. Chem.* **1996**, *100*, 1420–1425.

(29) Vanysek, P. In *CRC Handbook of Chemistry and Physics*, 93rd ed.; Haynes, W. M., Ed.; CRC Press/Taylor and Francis: Boca Raton, FL, 2013.

(30) Hanke, H. Molecular Simulations of the Water–Rutile Interface. Dissertation, Charles University, Prague, Czech Republic, 2011.

(31) Mamontov, E.; Wesolowski, D. J.; Vlcek, L.; Cummings, P. T.; Rosenqvist, J.; Wang, W.; Cole, D. R. Dynamics of Hydration Water on Rutile Studied by Backscattering Neutron Spectroscopy and Molecular Dynamics Simulation. *J. Phys. Chem. C* **2008**, *112*, 12334–12341.

(32) Marcus, Y. *Ion Properties*; CRC Press, 1997.

(33) Mills, R. Self-diffusion in normal and heavy water in the range 1–45°. *J. Phys. Chem.* **1973**, *77*, 685–688.

(34) Kohli, V.; Zhang, Z.; Park, C.; Fenter, P. Rb$^+$ and Sr^{2+} Adsorption at the TiO$_2$ (110)–Electrolyte Interface Observed with Resonant Anomalous X-ray Reflectivity. *Langmuir* **2009**, *26*, 950–958.

(35) Parfitt, G. D.; Ramsbotham, J.; Rochester, C. H. Infra-red study of hydrogen chloride adsorption on rutile surfaces. *Trans. Faraday Soc.* **1971**, *67*, 3100–3109.

(36) Seward, T. M.; Henderson, C. M. B.; Charnock, J. M.; Driesner, T. An EXAFS study of solvation and ion pairing in aqueous strontium solutions to 300°C. *Geochim. Cosmochim. Acta* **1999**, *63*, 2409–2418.

(37) Westall, J.; Hohl, H. A comparison of electrostatic models for the oxide/solution interface. *Adv. Colloid Interface Sci.* **1980**, *12*, 265–294.

(38) Sverjensky, D. A. Prediction of surface charge on oxides in salt solutions: Revisions for 1:1 (M$^+$L$^-$) electrolytes. *Geochim. Cosmochim. Acta* **2005**, *69*, 225–257.

(39) Sverjensky, D. A. Prediction of the speciation of alkaline earths adsorbed on mineral surfaces in salt solutions. *Geochim. Cosmochim. Acta* **2006**, *70*, 2427–2453.

(40) Ridley, M. K.; Hiemstra, T.; van Riemsdijk, W. H.; Machesky, M. L. Inner-sphere complexation of cations at the rutile–water interface: A concise surface structural interpretation with the CD and MUSIC model. *Geochim. Cosmochim. Acta* **2009**, *73*, 1841–1856.